

Energy for connected objects

Electromagnetic energy harvesting and wireless power transfer



Student: Fatine Azzabi

Date: 09/10/2025

Student: Gabriel Benveniste

Student: João Gabriel Button Albuquerque

1 Introduction

The main goal of this lab is to show the possibility to turn on a red LED ROHM SML-D12U1WT8 only using electromagnetic energy transmitted via radio waves or within the energy available in the environment. We have two strategies to do that : direct consumption and store-then-use. The first one means that the LED is lightened up by the captured energy. The second approach is the store-then-use strategy in which the energy is firstly stocked in a supercapacitor through a power management unit (bq25504 + TPS63031) before getting used to lighten up the LED.

As an application context of this type of wireless power supply we can mention sensors integrated into the concrete intended for Structural Health Monitoring (SHM) for monitoring the structure's state. Indeed, in this type of environment, it is usually impossible to change/replace the batteries of the device, thus it's crucial to develop autonomous sensors able to power themselves through ambient energy, specially from RF waves from nearby transmitters.

Beyond powering a simple LED, this lab aimed to characterise the entire wireless power chain, from the rectifier and PMU to the antenna and to identify real-world limitations such as non-linear effects, MPPT behaviour, and polarisation influence.

The experiments were thus designed not only to validate the theoretical energy calculations but also to observe how component tolerances and propagation conditions affect the actual performance.

This LAB was divided into three parts:

1. LED & Power Budget : this part includes the calculation of the necessary power for turning on the LED and determining the feasibility of both strategies (direct and store-then-use).
2. Rectifier characterisation : we had to measure the performances of RF rectifiers at 868 MHz and 2.45 GHz and conclude on its efficiency, bandwidth and optimal charge.
3. Antenna choice : this last part was about comparing different antennas to select the more adapted one for one specific application.

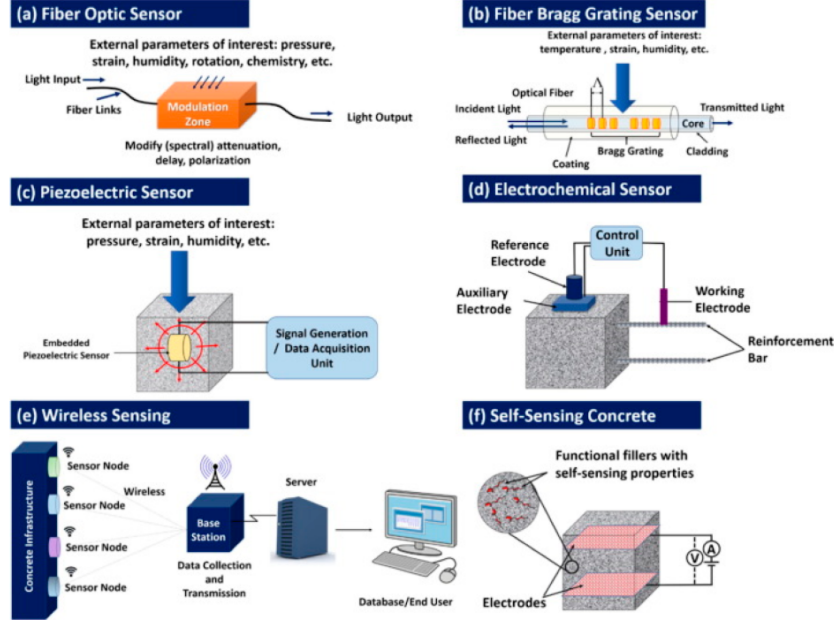


Figure 1: Example of an embedded sensor network for Structural Health Monitoring (SHM) in concrete
(source: MDPI Sensors, 2021)

Firstly, the energy harvesting consists of capturing a small amount of already present energy in the environment (such as light, heat, electromagnetic waves, vibrations...) and converting it into usable electricity. On the other hand, the wireless power transfer (WPT) relies on a wireless and contactless voluntary transmission of energy from a specific source toward a receptor.

Regarding the distance between the two, there can be either a nearby field transmission through an inductive or capacitive coupling (typically a few to several dozen centimetres, which corresponds to a short-range but still efficient transmission), or we can also have a distant field where the energy is transmitted through radiated electromagnetic waves, thus allowing it to reach several metres.

For our project, we're using radio frequency waves (RF) simply because they allow us to remote power supply while remaining compact and compatible with the ISM (Industrial, Scientific and Medical) bands at 868 MHz and 2.45 GHz, which are free to use. Hence, those frequencies range are a good option to have a nice range and efficiency but also a compact antenna size, which is what we are looking for when we are working with connected objects or integrated sensors (such as the one in concrete for the structure's following).

2 Theory

2.1 Power and Energy

The red diode that we will study in this lab is the *SML-D12V1W* from ROHM Semiconductors. From its datasheet table, useful information can be extracted (see highlighted content on Figure 1):

Ambient energy harvesting and wireless power transfer: focus on electromagnetic solutions

Near-field and far-field wireless power transfer				
Near-field		Far-field		
Capacitive coupling	Non-resonant inductive coupling	Resonant inductive coupling	Radiative (radiofrequency/microwave)	Laser
<ul style="list-style-type: none"> - Very short ranges - Very high voltages + Very good efficiency ($>90\%$) + Passes obstacles whose metal is insensitive + Misalignement insensitve + Little interferences ? Safety 	<ul style="list-style-type: none"> - Short ranges - Sensitive to metal - Sensitive to misalignement + Very good efficiency ($>90\%$) ? Safety 	<ul style="list-style-type: none"> - Short to medium ranges - Sensitive to metal - Sensitive to misalignement + Very good efficiency ($>90\%$) ? Safety + SWIPT 	<ul style="list-style-type: none"> + Large ranges + Good efficiency - Line of sight required - Interferences - Maturity - Electromagnetic compatibilities ? Safety + SWIPT 	<ul style="list-style-type: none"> + Very large ranges + Decent efficiency - Line of sight required - Interferences - Maturity ? Safety + SWIPT

Gaël LOUBET (gael.loubet@laas.fr)

Energy for Connected Objects

77 / 133

Figure 2: Principle of wireless power transfer in near and far field (5ISS course - Energy for IoT)

■ Specifications																		
Part No.	Chip Structure	Emitting Color	Absolute Maximum Ratings (Ta=25°C)						Electrical and Optical Characteristics (Ta=25°C)									
			Power Dissipation P _D (mW)	Forward Current I _F (mA)	Peak Forward Current I _{FP} (mA)	Reverse Voltage V _R (V)	Operating Temp. T _{opt} (°C)	Storage Temp. T _{stg} (°C)	Forward Voltage V _F Typ. (V)	Reverse Current I _R Typ. (mA)	Max. (mA)	V _R (V)	Dominant Wavelength λ _D Min.*2 (nm)	Max.*2 (nm)	I _F (mA)	Luminous Intensity I _V Min. (mcd)	Typ. (mcd)	I _F (mA)
SML-D12V1W	AlGaN/P	Red	54	20	100*1	5	-40 ~ 85	-40 ~ +100	2.2	20	10	5	625	630	635	25	40	20
SML-D12U1W		Orange											615	620	625	40	63	
SML-D12D1W		Yellow											602	605	608	587	590	593
SML-D12Y1W		Yellow-green											569	572	575	16	30	
SML-D12M1W																		

*1:Duty1/10, 1kHz *2:Measurement tolerance: ±1nm

Figure 3: Specifications for SML-D12x1 Series, ROHM Semiconductors

- **Forward current rating** $I_F = 20mA$ (continuous).
- **Forward voltage** (typical) at $I_F = 20mA$: 2.2V
- **Power dissipation limit** $P_D = 54mW$

Note that conditions (current, voltage) to obtain this power dissipation limit are not displayed in the datasheet.

The electrical DC power can be expressed as $P = I_F \cdot V_F$, and the energy for 1 second as $E = P \cdot t$. Operating points can be extracted from the datasheet graphics (see Figure 2):

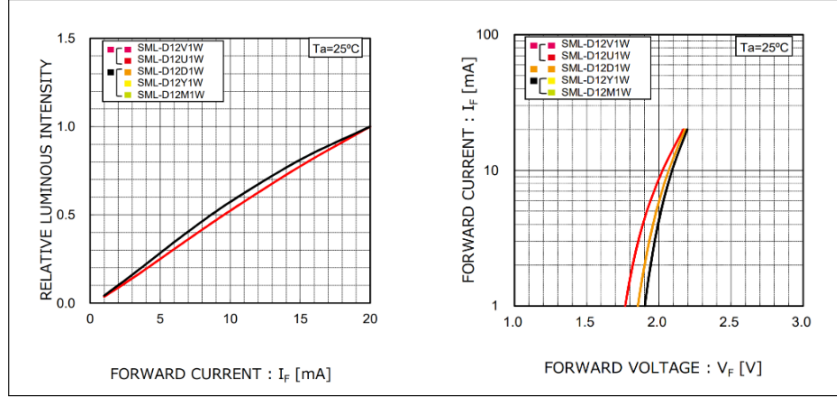


Figure 4: Luminous Intensity - Forward Current (Left), Forward Current - Forward Voltages (Right)

Theoretical results obtained from the data-sheet, can be merged into the following table:

Brightness (%)	Power (mW)	Energy (mJ)
100	44	44
50	19	19
25	9	9

Table 1: Power and Energy for the LED, different luminous intensities

Note that brightness and power (or energy) are not proportional, since luminous intensity vs current is not linear (but close) and the same applies to current vs voltage.

2.2 Consumption strategies

To light up the LED for *1 second*, two strategies can be used: lighting the LED directly from the rectifier (**direct**), or accumulating energy and then driving the LED at a controlled voltage/current (**store-then-use**).

- With **direct consumption**, the chain is quite simple: antenna → rectifier → LED. The response is immediate, but the LED current and brightness depend on the instantaneous RF field. The wave intensity also depends on the distance between the device and the power source (antenna). Because the power propagation is in a "donut" format, the farther the device is from the source, the less energy it receives. To ensure that the LED has a specific brightness for a specific amount of time, the ideal setup must store the minimal energy to power the LED for 1 second as wanted.
- With **store-then-use** (PMU + DC-DC + supercapacitor), the chain contains more elements: antenna → rectifier → PMU (*bq25504 PMU*) → storage (supercapacitor) → buck-boost (*TPS63031*) → LED. This system accumulates energy until there is enough to run the LED at a fixed current/-voltage. Factors such as cold-start, activation and deactivation voltage thresholds, and maximum capacitor losses must be considered (see §2.3).

The Power Management Unit (TI BQ25504) defines two thresholds: $V_{min} = 2.2 \text{ V}$ and $V_{max} = 5.25 \text{ V}$. It performs a Maximum Power Point Tracking (MPPT) routine every $\sim 14 \text{ s}$ by sampling the open-circuit voltage and adjusting its input impedance to about 40% of V_{oc} . This periodic sampling explains the voltage oscillations observed later in the experimental measurements.

2.3 Supercapacitor options

A capacitor stores energy $E = \frac{1}{2} \cdot C \cdot V^2$. A Power Management Unit (PMU) allows a discharge down to V_{min} and a charge up to V_{max} . The stored energy per cycle is called the usable energy:

$$E = \frac{1}{2} \cdot C(V_{max}^2 - V_{min}^2).$$

Since those threshold values and the stored energy are known, as seen in the previous section, it is easy to choose the right capacitor. For example, to store $44mJ$ at normal brightness with the given thresholds, the necessary capacitor has a value of $C = 3.9mF$. This capacitor is not on the given list of available capacitors, so the following one is taken, at $6.8mF$. If a bigger capacitor is chosen, thresholds must be adjusted to ensure that the equation remains valid.

How to fix V_{min} and V_{max} then? Since there is more energetic depletion with a higher voltage, the best way is to fix those thresholds as low as possible to reduce depletion. By doing so for each case (100%, 50% and 25%), the following table is obtained:

Brightness (%)	Energy (mJ)	Capacitor (mF)	Thresholds (V)	Max. losses (μW)
100	44	6.8	2.2 - 4.2	70
50	19	2.2	2.2 - 4.8	650
25	9	1.5	2.2 - 4.1	430

Table 2: Capacitor values

Note that these choices keep the discharge floor as low as the PMU allows ($2.2V$) to maximise usable ΔV^2 . Plus, max losses for each capacitor are not proportional to the amount of energy stored. They depend on capacitor technology (electro-lytic, electrochemical...).

It was observed that energy stored below V_{min} cannot be used by the PMU, resulting in “dead” energy. Larger capacitors store more total energy but also increase the charging time and the amount of unused energy. During the lab, the 6.8 mF capacitor required significantly longer to reach V_{max} than the 1.5 mF one, confirming this trade-off.

2.4 Rectenna fundamentals

In radiative WPT/RF harvesting the receiver is a rectenna. That is an antenna that captures RF power, an impedance-matching network that maximises power transfer, a non-linear rectifier (diode/transistor) that converts RF to DC, and a DC smoothing/storage stage. Co-optimising these blocks is essential. Note that the “best” antenna and the “best” rectifier in isolation do not yield the highest end-to-end efficiency together.

Selection is made by the operating band (868 MHz or 2.45 GHz in ISM), bandwidth, gain/pattern (omni vs directional), size, input impedance, and polarisation match to the transmitter.

The antenna type and polarisation have a direct influence on the harvested power. Linear-polarised antennas are sensitive to alignment: a 90° rotation between transmitter and receiver reduces the received power roughly by 50%. Circularly-polarised antennas would mitigate this effect in multipath environments. In this lab, both 868 MHz and 2.45 GHz bands were investigated.

3 Experiments

In the previous sections we've studied the architecture configuration for each energy objectives, 100%, 50% and 25% brightness. Our group was randomly provided with a "white box" device containing a 2.2 nF capacitor. Based on the previous studies (results of Table 2), we can deduct that it corresponds to the 50% brightness LED configuration. With this device in hands, our goal is to characterise the optimal rectifier frequency of this device, in order to identify its operating behaviour and the wireless power frequency, so we can see in witch frequency the device is more efficient wireless charging.

In this context, we are going to connect two devices to the board under study. One of this devices will act as a transmitter, sending energy at various frequencies, while the other will be used to observe the signal after the rectifier, showing the energy (in volts) obtained from the signal. Because we are working in high frequencies ($> 2\text{ GHz}$), we are not able to use a normal oscilloscope to observe the signal, for example, we need a more specific device. In a specific case like this, involving high frequencies and without using expensive equipment, our group was provided with the [Ettus USRP B200 mini](#) and the [Analog Discovery 3](#), both connected to a Raspberry Pi 4, which is responsible for running the specific software required to control each device, GNU Radio and WaveForms respectively. The resulting experimental setup is illustrated in Figure 3.

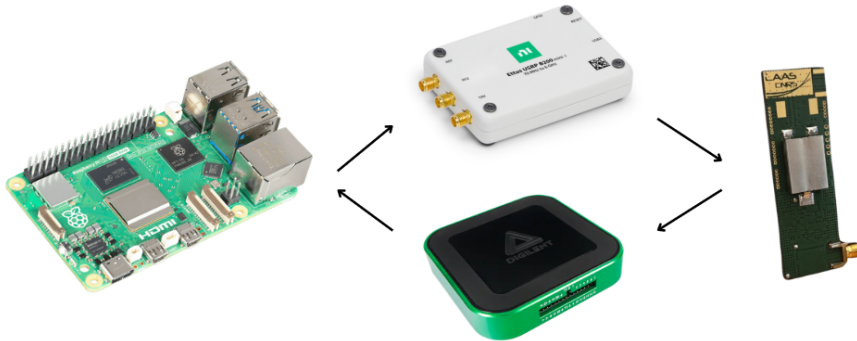


Figure 5: Experimental setup architecture

For this initial study, we are not going to use an antenna to send the energy signals. Because we are doing an initial frequency studies, we need the input signals to be as clean as possible and in the frequency that we want to study. This means that we don't want parasite ambient frequencies, for example, we want very efficient transfer of power from the source to the device. To do so, we've connected the Ettus USRP B200 Mini to the device in study with RF coaxial cable, which is similar to an fiber optic cable that directs the signal to the device.

The load was fixed at $1.5\text{ k}\Omega$ and the RF input power at 15 dBm (corresponding to a USRP gain of 73). Each frequency point was held for $\sim 16\text{ s}$ to allow the MPPT routine to stabilise before recording the voltage. All connections were first made through coaxial cables to eliminate parasitic effects, antennas were used later for over-the-air tests.

In the first 2 experiments, the Ettus USRP B200 Mini is used to generate the desired signal while performing a frequency sweep between 800 MHz and 950 MHz, and between 2.4 GHz and 2.5 GHz, with a frequency step of 10 MHz. The signal is applied to a resistive load of $1.5\text{ k}\Omega$ with an RF input power of -15 dBm , corresponding to a 74 gain in GNU Ration. Using the Analog Discovery 3, we are able to analyse the resulting energy signals after the rectifier. This experiments gives the results showed in Figures 4 and 5.

Furthermore, to evaluate the system's response over a broader frequency range and verify whether the device is optimised only for the target bands, or if it also harvests energy at other frequencies, we extended the sweep from 70 MHz to 3 GHz with a step of 100 MHz. This third experiment gives the results showed in Figure 6.

In the final part of the session, coaxial links were replaced with antennas in order to characterise the influence of radiation, distance, and polarisation on the harvested energy.

4 Results and discussions

In this section we are going to take a look at the results of each experiment and analyse the corresponding curves / signal outputs seen in WaveForms that correspond to the energy obtained for each frequency. Also discussing the conclusions of each signal response.

4.1 Experiment 1: 800 MHz to 950 MHz, step of 10 MHz

We can see in Figure 4 that the curves obtained in the experiment shows that we have a decreasing energy gain in relation to the frequency. If our device had been designed to operate at 868 MHz, we should have seen a increase of obtained power neat this frequency. We can also consider that the device is not perfect and the working frequency might have changed / dislocated to a smaller frequency (because we have more power in smaller frequencies).

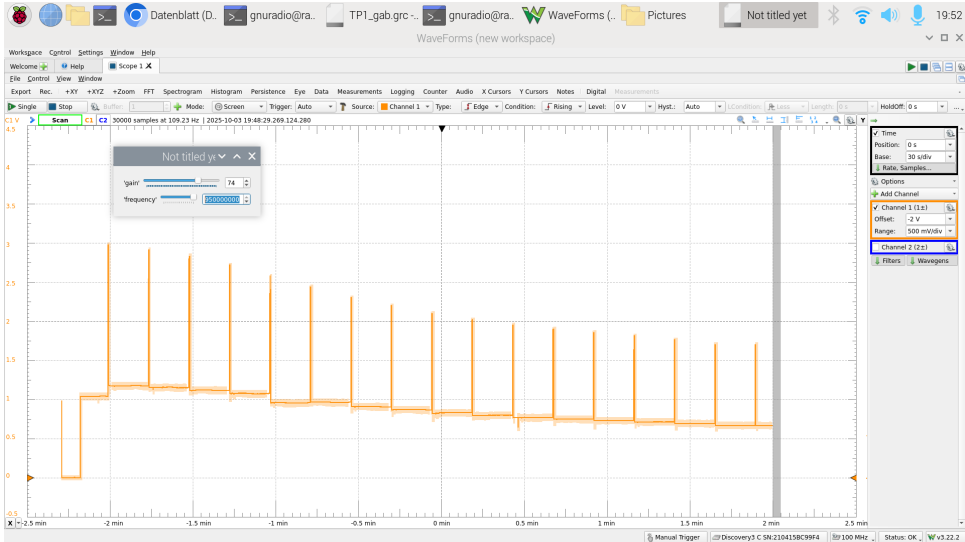


Figure 6: Experiment 1: 800 MHz to 950 MHz

4.2 Experiment 2: 2.4 GHz to 2.5 GHz, step of 10 MHz

We can see in Figure 5 that the power obtained in this range of frequency is bigger then the one obtained in the previous experiment and also that it's a steady curve. This means that we've found the optimal wireless charging frequency of the device, where it can obtain more power then 868 MHz with the same gain. Also that we've a range of frequencies that we can charge our device, with we'll see more clearly in the results of the next experiment.

Periodic fluctuations of the measured voltage (every ~ 14 s) were observed, corresponding to the MPPT open-circuit sampling described earlier.

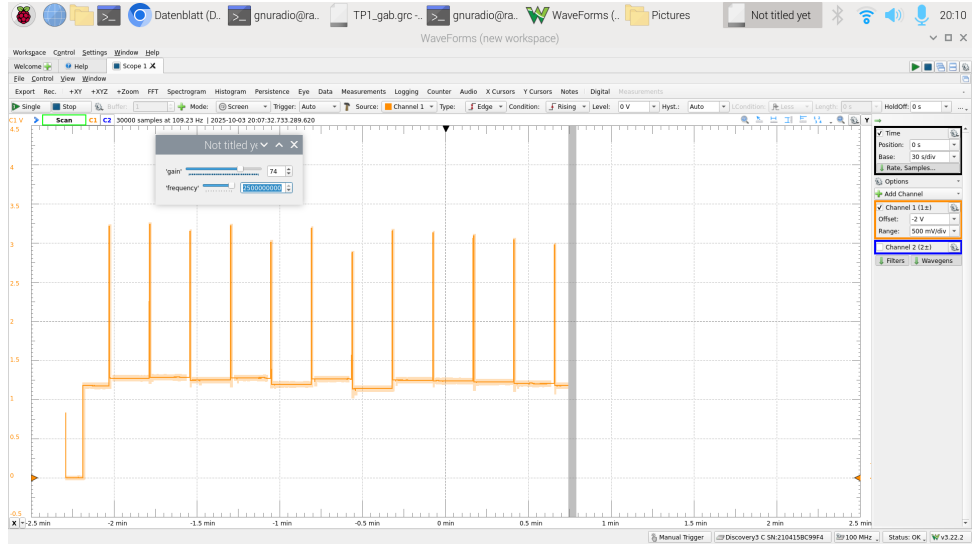


Figure 7: Experiment 2: 2.4 GHz to 2.5 GHz

4.3 Experiment 3: 70 MHz to 3 GHz, step of 100 MHz

If 868 MHz or 2.4 GHz were the ideal frequency, we would expect to see a band-pass behaviour around this frequencies, with a bigger amplitude. We can see this behaviour more clearly and with a bigger amplitude, meaning more energy received, in the 2.4 GHz frequency band. So we can conclude that our was built to work on this frequency. Even though the device was built to work on a specific frequency range, parasitics elements, coupling effects and non-linearities cause other frequencies to influence its overall behaviour.

The shift of the resonance peak when changing the input power confirms the non-linear behaviour of the diode rectifier. Component tolerances and PCB parasitics also contribute to these small frequency shifts.

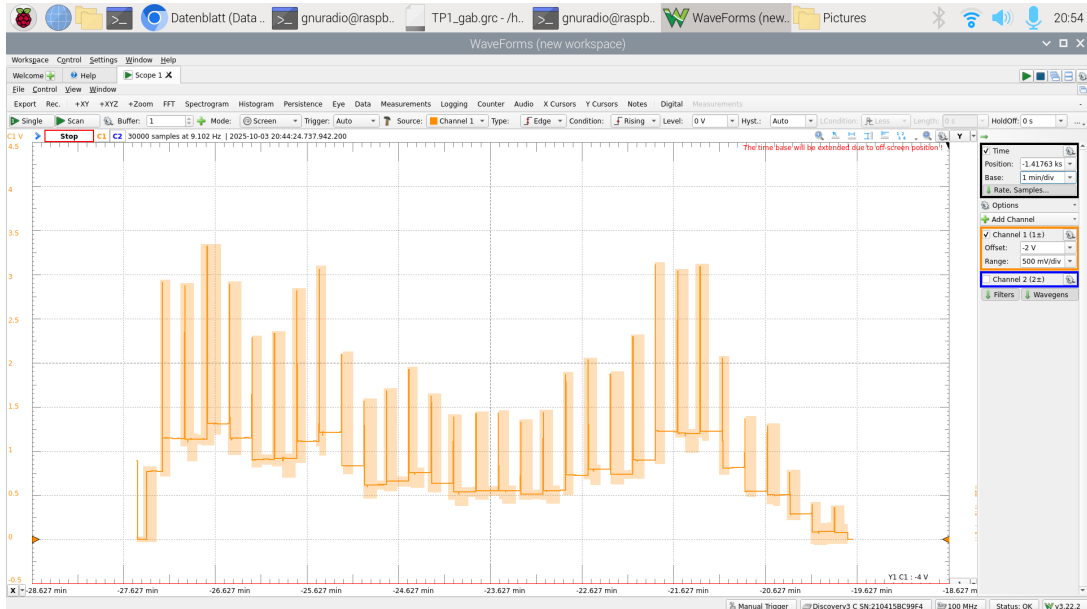


Figure 8: Experiment 3: 70 MHz to 3 GHz

4.4 Antenna and Polarisation Effects

After the coaxial characterisation, the system was tested over-the-air using 868 MHz and 2.45 GHz antennas.

At equal transmitted power (-15 dBm), the 2.45 GHz horn antenna provided the highest rectified voltage, while the 868 MHz patch showed lower output due to narrower bandwidth.

Rotating the receiving antenna by 90° reduced the rectified voltage by about half, confirming the sensitivity to polarisation alignment. The vertical orientation was more stable indoors, whereas the horizontal one suffered from reflections and depolarisation.

These results underline that antenna gain, alignment, and polarisation are key parameters in wireless power transfer efficiency.

4.5 MPPT Behaviour and Power Variation

The BQ25504 PMU periodically interrupts its input every $\sim 14 \text{ s}$ to sample V_{OC} (Voltage open circuit) and sets the operating point at 40% V_{OC} . This explains the voltage oscillations observed on the oscilloscope.

When the available RF power dropped below -18 dBm , the PMU could not start, defining the minimum power required for cold-start operation.

4.6 Ambient Harvesting and Wireless Power Transfer

This part of the work was not carried out during the lab due to time limitations. However, the instructor explained that ambient electromagnetic power levels are far too low to power a LED directly.

In practice, only a dedicated transmitter placed very close to the receiver can provide enough energy.

During the experiments, we observed that the LED could only turn on when the distance to the source was within a few tens of centimetres, confirming that ambient harvesting alone is not sufficient for this kind of application.

5 Conclusion

This lab demonstrated the complete characterisation of a wireless power transfer chain for low-power IoT applications.

Both direct consumption and store-then-use modes were validated, confirming theoretical energy requirements of 44 mJ, 19 mJ and 9 mJ for 100 %, 50 %, and 25 % brightness respectively.

The rectifier performed best near 2.45 GHz, showing a wide operating plateau, while the 868 MHz version delivered lower output.

The MPPT routine of the BQ25504 ($P \sim 14$ s cycle at 40 % V_{OC}) was clearly observed. Antenna alignment and polarisation strongly affected received power, a 90° rotation causing roughly 50 % loss.

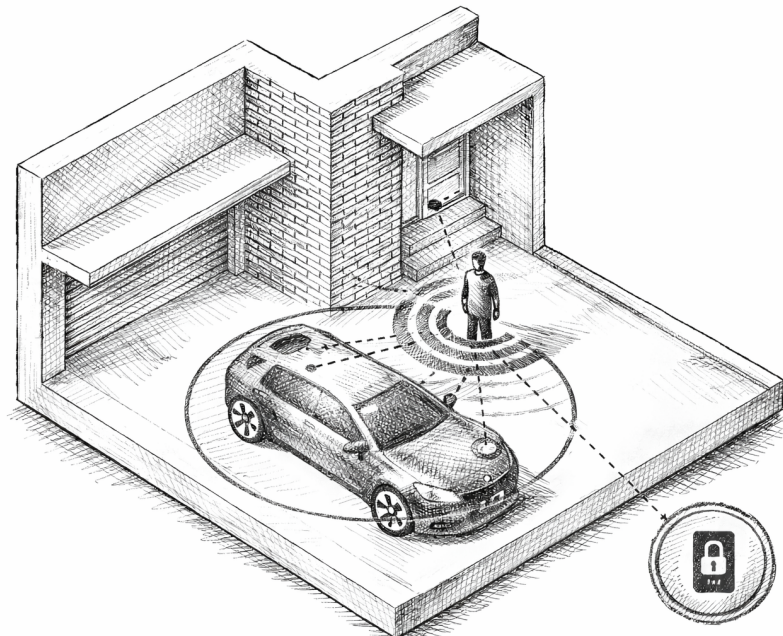
These results confirm that the performance of wireless power transfer systems depends as much on circuit design as on antenna parameters and environmental conditions.

Future improvements could include circularly-polarised or dual-band antennas, adaptive matching networks, and optimised supercapacitors to extend range and stability.

Keyless Entry in Automotive

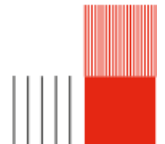
A Energy focus study

Amine Benchekroun
Badr Diani
Fatine Azzabi
João G. Buttow A.



Institut National des Sciences Appliquées de Toulouse

January 20, 2026



Contents

Introduction	2
Energy Management Objectives and Design Constraints	3
Energy measurement approaches	4
Shunt-Resistor Measurement Setup	5
Results 1 – Initiator	6
Results 2 – Receptors	7
Latency	7
Power Consumption and Battery Autonomy	8
Measurement Context	8
Per-Node Current Model	8
System Power and DC–DC Conversion	9
Battery Assumptions and SoC/DoD Limits	9
Autonomy Results	9
Smartphone Energy Considerations	10
Fleet Operation and Energy Availability	11
Battery Constraints	11
Mitigation Strategies	11
1. Auxiliary-battery autonomy example (LiFePO ₄ 12.8 V – 30 Ah)	11
2. Rooftop Solar Charging	12
Conclusion	14

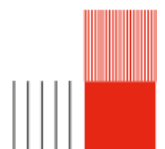


Introduction

In recent years, the rapid integration of connected technologies into vehicles has transformed how users interact with mobility systems, especially in corporate fleets. Beyond tracking and logistics, fleet platforms increasingly incorporate intelligent access mechanisms that improve usability and operational efficiency while maintaining strong security requirements. Within this context, our project, developed in collaboration with ACTIA, investigates a keyless access solution for company vehicles based on embedded devices and short-range wireless communication.

The proposed architecture relies on a distributed in-vehicle infrastructure composed of a central unit and four anchor nodes located at the vehicle corners. The employee smartphone acts as the user credential and interacts with the vehicle through a two-layer approach: Bluetooth Low Energy (BLE) provides a low-power presence and wake-up mechanism, while Ultra-Wideband (UWB) is used for short, explicit ranging phases when accurate localization is required. This tiered strategy is intended to reduce unnecessary radio activity while keeping the access experience responsive when the user approaches the vehicle.

Such a design introduces a key engineering constraint: energy must be carefully managed on both sides of the system. On the user side, continuous scanning and frequent ranging operations can impact smartphone autonomy. On the vehicle side, the in-vehicle nodes draw power from the low-voltage electrical system and must remain available without compromising the ability to start the vehicle, even after extended parking periods. For this reason, this report focuses on an energy-oriented study of the access system. We (i) define the main energy-management objectives and constraints, (ii) describe the measurement approaches used to characterize current consumption (power analyzer baseline and shunt-resistor measurements with an oscilloscope), (iii) report experimental results for initiator and responder behaviors, including the observed latency range, and (iv) estimate the resulting battery autonomy under conservative state-of-charge constraints. Finally, we discuss fleet-operation scenarios and propose mitigation strategies to preserve energy availability during long idle periods, including the use of an auxiliary battery and rooftop photovoltaic charging.



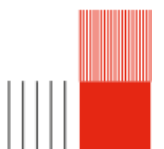
Energy Management Objectives and Design Constraints

Energy management in a keyless fleet-access system must reconcile three competing objectives: (i) maintaining a responsive and fluid user experience, (ii) preserving the autonomy of the employee’s smartphone, and (iii) ensuring continuous availability of the in-vehicle embedded infrastructure. Unlike conventional access solutions that only consume energy during short user actions (e.g., pressing a remote key fob), connected access systems create background activity: advertising, scanning, connection establishment, ranging exchanges, and periodic status checks. If left unconstrained, these operations can introduce unnecessary energy drain, especially on the smartphone side where battery capacity is limited and shared with other user activities.

The design is therefore driven by the following constraints:

- Smartphone autonomy constraint: the phone must not remain in continuous high-power scanning or ranging states. The access mechanism should remain opportunistic and proximity-triggered, so that energy consumption remains negligible when the user is far from the vehicle.
- Vehicle-side availability constraint: the embedded system must remain reachable at all times. However, the car battery should not be significantly affected by the access infrastructure, particularly for vehicles parked for long periods.
- Responsiveness constraint: when the user approaches, the system must “wake up” quickly enough to keep the experience seamless (no long waiting time at the door).
- Reliability and robustness: the system must tolerate intermittent radio conditions, temporary packet loss, and user motion dynamics without falling back to energy-expensive behaviors (e.g., repeated ranging bursts).
- Security compatibility: energy-saving modes must not weaken authentication guarantees; in particular, low-power behavior must not bypass cryptographic steps or allow uncontrolled repeated attempts.

To address these constraints, the project adopts a tiered activation strategy: BLE is used as a low-energy “presence and wake-up” layer, while UWB is reserved for short, explicit localization phases where precise ranging is required.



Energy measurement approaches

Our first approach for the energy study was to perform direct power measurements using the HMC8015 Power Analyzer made available by our project supervisor. The plan was to power the different hardware configurations through the analyzer and quantify the consumption in representative scenarios, as illustrated in Figure 1a. In practice, we intended to perform measurements both on the user side and on the vehicle side, starting from simplified configurations (one transmitter and one receiver) and progressively moving to the complete architecture (the four UWB anchors and the central unit on the vehicle side, together with the user board), in order to capture the incremental contribution of each element.

To validate the setup and obtain a reference point, we first conducted baseline tests on the boards in idle conditions, i.e., powered on but without any application running. These measurements were successfully obtained by connecting the boards to the HMC8015 and recording the values displayed by the instrument (Figure 1b). In this configuration, the analyzer indicates an input voltage of approximately 233 V and an RMS current of 12.33 mA, corresponding to an electrical power of 0.810 W. With these readings, it becomes possible to estimate the average power consumption of the device in this operating mode, providing a baseline reference for later comparisons with more active phases of the system.



(a) Test Bench Setup for Power Consumption Measurement

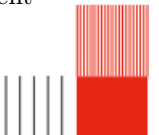


(b) Readings during test

Figure 1: Power-consumption measurement using HMC8015 Power Analyzer.

However, when attempting to extend the measurements to realistic operational phases—such as UWB transmission, reception, and ranging exchanges—we faced a practical limitation of the experimental setup. In our implementation, the UWB boards cannot run autonomously for these operations: they must remain connected to a computer that provides the required libraries and packages, and the communication procedures are controlled through a Python-based workflow executed on the host machine. This dependency exists both on the user side and on the vehicle side, meaning that the active radio behavior cannot be isolated as a standalone embedded workload powered exclusively through the analyzer.

As a consequence, the measurement configuration no longer represents the system's true operating conditions: the boards are simultaneously influenced by the host connection and by the execution flow controlled externally, and the instrumentation available in the course does not allow us to separate the consumption strictly associated with the UWB radio activity from the overall setup. Given these constraints, it was not possible to obtain reliable and reproducible consumption values during emission/reception phases using our measurement tools. Therefore, we decided to shift our approach. After consulting other professors and examining measurement practices in the scientific literature, we found that placing a shunt resistor on the USB power line feeding the board enables the most accurate current measurement, and thus the most reliable energy consumption estimate.



Shunt-Resistor Measurement Setup

To estimate the energy consumption of the NXP UWB boards under realistic operating conditions, we adopted a non-intrusive current-measurement method based on a shunt resistor. The goal was to avoid modifying the board hardware (and therefore reduce the risk of damage), while still measuring the supply current drawn from the USB 5 V line.

The USB cable was cut and a shunt resistor was inserted in series with the +5 V supply wire. Using a differential probe and an oscilloscope, we measured the voltage drop across the shunt resistor and deduced the current using Ohm's law:

$$I(t) = \frac{V_{\text{shunt}}(t)}{R_{\text{shunt}}}.$$

The welding operation and the modified cable are illustrated in Figure 2.



Figure 2: Insertion of the shunt resistor into the USB power cable.

We initially selected a 6.8Ω shunt resistor to obtain a larger measurable voltage drop and improve the signal-to-noise ratio. However, this value introduced a significant voltage drop (approximately 0.7 V), which reduced the effective supply voltage seen by the board and prevented the responder nodes from operating reliably. To mitigate this issue, we replaced the shunt with a smaller resistance (1.3Ω), reducing the voltage drop while keeping sufficient measurement resolution. The final experimental setup is shown in Figure 3.

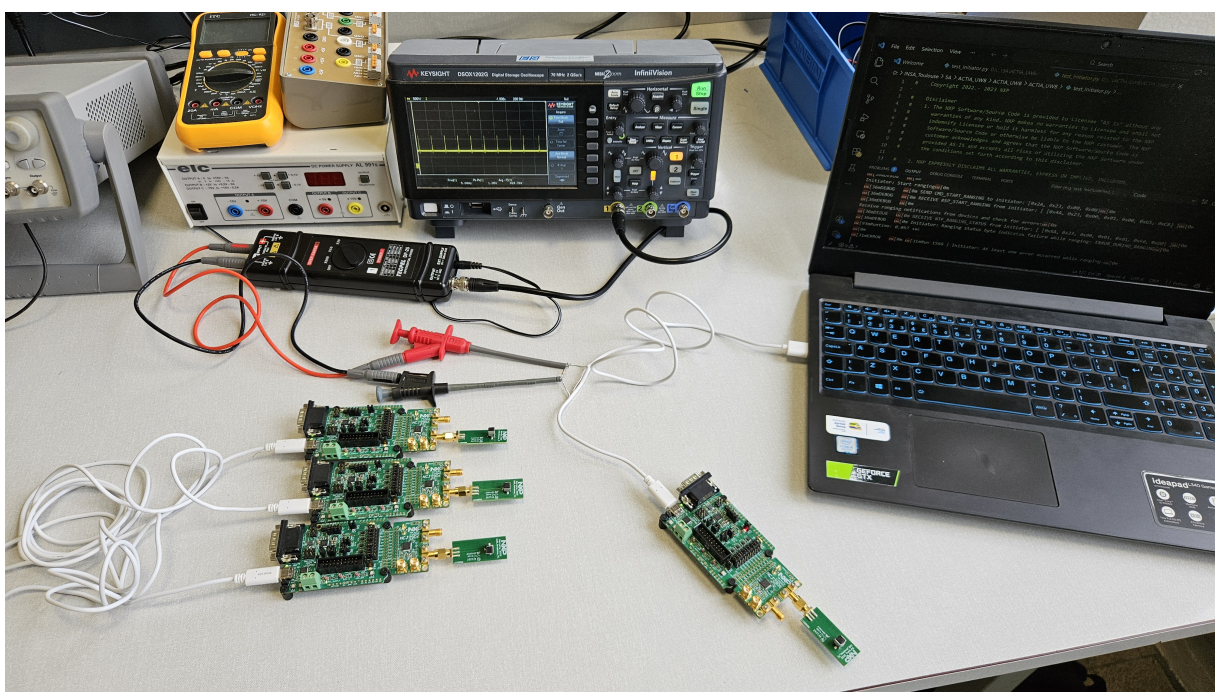


Figure 3: Final measurement setup with a 1.3Ω shunt resistor, differential probe, and oscilloscope.



Using this setup, we evaluated two representative configurations. First, we performed an initiator-side measurement, where the initiator board (representing the smartphone) was placed approximately 20 cm from the responder boards. Second, we conducted a responder-side measurement using three responder boards; only one of them was powered through the shunt cable in order to capture its current profile. For this second configuration, measurements were carried out at both 20 cm and 5 m, which corresponds to the distance range where the system begins the transition from BLE-based detection to UWB ranging.

Results 1 – Initiator

Figure 4 compares the initiator current consumption in two conditions: (i) idle mode (board powered, no application running) and (ii) active mode (UWB communication enabled, code running). The measured average current increases from 92.3 mA in idle mode to 109.3 mA during communication.

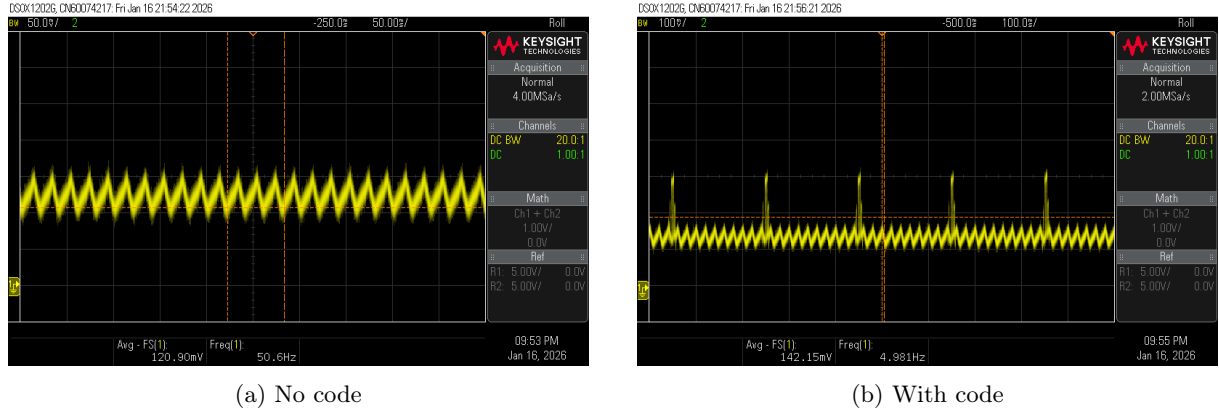


Figure 4: Initiator consumption

The increase in average current between the idle case (no code) and the active case (with code) is mainly explained by the additional energy required for UWB ranging transactions. When the application is running, the initiator periodically triggers a ranging exchange with each responder. This generates short bursts of current corresponding to RF transmission/reception, digital processing, and SPI activity inside the UWB transceiver.

This behavior is visible in Figure 5, where three distinct current peaks appear. These peaks are consistent with the fact that three responder boards are present in this experiment: the initiator performs a separate ranging sequence for each responder, leading to one current burst per responder within a given cycle. Between these bursts, the board returns to a lower-power state, which explains why the overall current waveform alternates between a baseline level and short high-current events.

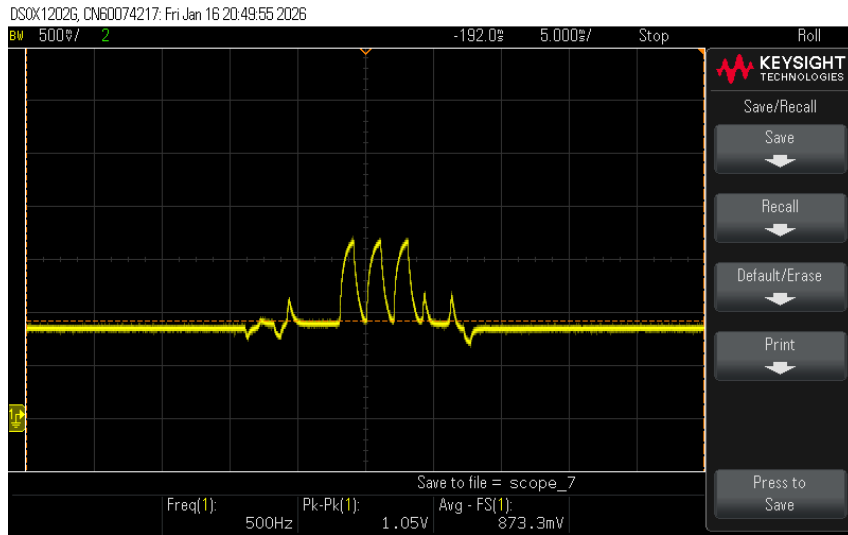


Figure 5: 3 Current pics



Therefore, the higher mean current measured in the communication mode does not come from a constant increase in power consumption, but from the accumulation of these repeated high-current pulses associated with UWB exchanges. The more frequent the ranging cycles (or the higher the number of responders), the greater the average current will become.

Results 2 – Receptors

Figure 7 compares one responder (receptor) consumption for two distances from the initiator: (i) short range at 20 cm and (ii) long range at 5 m. From the oscilloscope average shunt-voltage values, we observe an increase from about 151 mV at 20 cm to about 210 mV at 5 m, indicating a higher average current at a longer distance (using the shunt-resistor method introduced in the measurement setup).

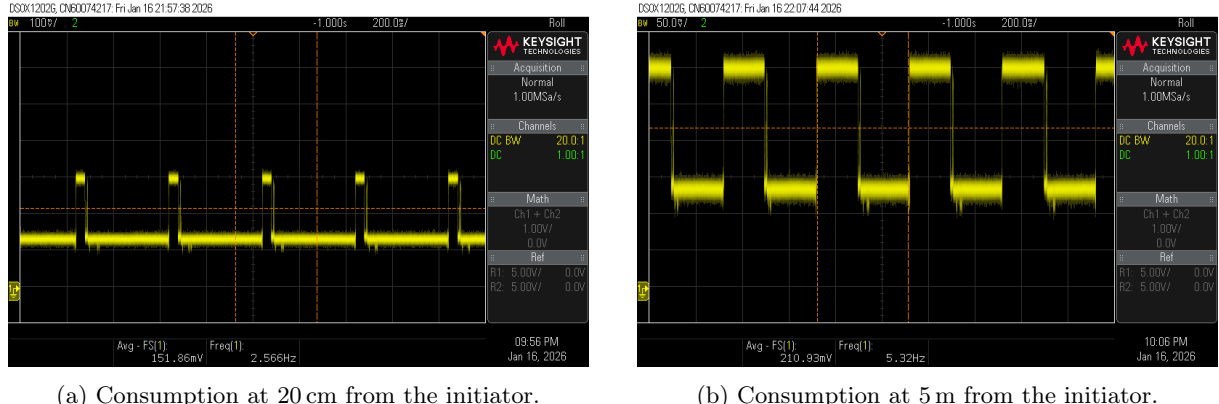


Figure 6: Consumption of the receptors (responders) for two initiator distances.

As in the initiator measurements, the responder waveform is not constant: it alternates between a lower baseline level and repeated higher-consumption phases. These active phases correspond to the responder being periodically awakened to participate in UWB ranging transactions (receive windows, response transmission, and internal processing within the UWB transceiver). Between two transactions, the board returns to a lower-power state, which explains the square-like duty-cycled shape visible in Figure 6a and Figure 6b.

A key difference between the two cases is the activity rate and duty cycle. At 20 cm (Figure 6a), the oscilloscope indicates a repetition frequency of about 2.6 Hz, with an average shunt voltage of $\bar{V}_{\text{shunt}} \approx 151 \text{ mV}$. At 5 m (Figure 6b), the repetition frequency increases to about 5.3 Hz and the average shunt voltage rises to $\bar{V}_{\text{shunt}} \approx 210 \text{ mV}$. This higher mean level is consistent with a more demanding radio link at longer distances: degraded signal quality can increase the time spent in active listening and may require additional retries, effectively increasing the duty cycle of the high-consumption phases.

Therefore, the increase in average consumption at 5 m is mainly explained by the accumulation of more frequent and/or longer active UWB communication periods, rather than a purely constant shift of the baseline current.

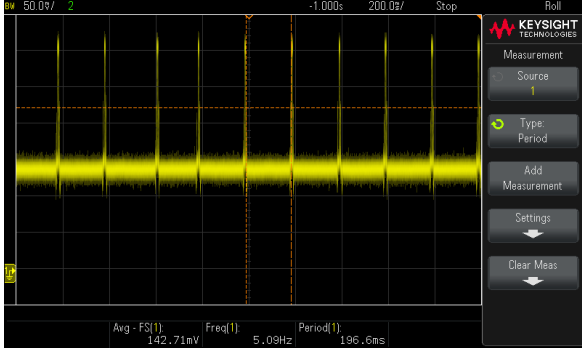
Latency

To characterize system responsiveness, we extracted timing information directly from the runtime logs produced when executing our UWB ranging code and from the current-consumption measurements, where transmit/receive events can be identified from the corresponding current peaks. On the transmitter side, the emission period was configured and observed as constant at 200 ms (i.e., 5 Hz). This value was confirmed in two independent ways: (i) by the timestamps in the execution logs, and (ii) experimentally using the oscilloscope, where the current-draw peaks associated with UWB transmissions appear with the same 5 Hz repetition rate (Fig. 7a).

On the receiver side, the effective reception/update period was not constant and depended on link conditions. Based on the log timestamps, the receiver period varied between approximately 200 ms and 500 ms. This variability is also visible in the oscilloscope measurements: the spacing between current-consumption peaks on the receiver is not uniform, which corroborates that the reception timing (and thus the perceived latency) varies in practice (Fig. 7b).

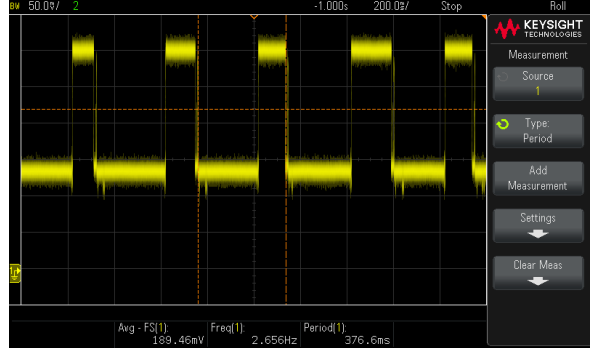


DSOX1202C CH60074217 Fri Jan 16 22:10:03 2026



(a) Period emission

DSOX1202C CH60074217 Fri Jan 16 22:11:36 2026



(b) Period reception

Figure 7: Period of the emission and reception

Power Consumption and Battery Autonomy

Measurement Context

We experimentally characterized the average current consumption of the NXP UWB development platforms under representative operating conditions. As commonly observed with development kits, the measured consumption is not only determined by radio activity but also by on-board peripherals and development-oriented circuitry (such as debug interfaces, indicator LEDs, and auxiliary regulators) that are not strictly required in a final embedded product. In our setup, we were unable to selectively disable all auxiliary subsystems while maintaining a realistic communication workflow. Therefore, for system-level autonomy calculations, we adopt a deployment-oriented assumption: in a fleet-scale implementation, each node would be built on a dedicated minimal hardware design whose purpose is limited to BLE/UWB communication, reducing the baseline current compared to a development board. This modeling choice is aligned with usage recommendations for automotive lead-acid starter batteries, for which deep discharges are discouraged because they accelerate aging and reduce service life [17, 6].

Per-Node Current Model

From our measurements, enabling UWB transmission increases the average board current from 92 mA (non-transmitting condition) to 210 mA, i.e., an incremental draw of approximately 118 mA. We further assume a minimalistic communication-oriented baseline of 40 mA for a dedicated custom board. Finally, since we could not directly estimate the operational current consumption of the BLE subsystem, we rely on the measurements reported by Garcia *et al.*, which evaluate multiple commercial BLE platforms under a 100 ms connection interval in the peripheral role: the NXP FRDM-KW41Z averages approximately 0.118 mA, while other platforms range from 0.067 mA to 0.279 mA under the same latency configuration [7]. To estimate energy consumption in a worst-case scenario while adding a small safety margin, we model BLE consumption as a conservative average of 0.3 mA for a 100 ms connection interval.

Two operating cases are considered:

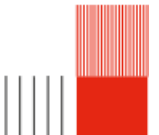
Case A (BLE only / UWB not continuously active):

$$I_{\text{node,A}} = I_{\text{base}} + I_{\text{BLE}} \approx 40 \text{ mA} + 0.3 \text{ mA} = 40.3 \text{ mA}, \quad (1)$$

Case B (BLE + UWB continuously active):

$$I_{\text{node,B}} = I_{\text{base}} + I_{\text{UWB}} + I_{\text{BLE}} \approx 40 \text{ mA} + 118 \text{ mA} + 0.3 \text{ mA} = 158.3 \text{ mA}. \quad (2)$$

To avoid unnecessary standby consumption, cloud connectivity is assumed disabled when the vehicle is OFF (no need to maintain an active backhaul link). Moreover, we do not include the power draw of the vehicle on-board computer/infotainment, as it is highly model-dependent and would require OEM-level specifications to estimate credibly.



System Power and DC–DC Conversion

The system comprises five nodes located inside the vehicle (four at the extremities and one at the center). Each node is supplied at 5 V. The per-node and total load powers are:

$$P_{\text{node}} = V_{\text{load}} I_{\text{node}}, \quad (3)$$

$$P_{\text{tot}} = N P_{\text{node}} = N V_{\text{load}} I_{\text{node}}, \quad N = 5, \quad V_{\text{load}} = 5 \text{ V}. \quad (4)$$

For Case A (Eq. 1):

$$P_{\text{node,A}} = 5 \cdot 0.0403 = 0.2015 \text{ W}, \quad (5)$$

$$P_{\text{tot,A}} = 5 \cdot 0.2015 = 1.0075 \text{ W}. \quad (6)$$

For Case B (Eq. 2):

$$P_{\text{node,B}} = 5 \cdot 0.1583 = 0.7915 \text{ W}, \quad (7)$$

$$P_{\text{tot,B}} = 5 \cdot 0.7915 = 3.9575 \text{ W}. \quad (8)$$

Since the vehicle battery is nominally 12 V and the electronics require 5 V, a DC–DC buck converter is required. Converter efficiency depends on the operating point; modern automotive buck modules can reach high efficiencies for 12 V to 5 V conversion, and we adopt a representative value of $\eta = 0.90$ [14]. The equivalent current drawn from the battery is then approximated by a power balance:

$$I_{\text{bat}} \approx \frac{P_{\text{tot}}}{\eta V_{\text{bat}}}, \quad V_{\text{bat}} = 12 \text{ V}. \quad (9)$$

Thus,

$$I_{\text{bat,A}} = \frac{1.0075}{0.90 \cdot 12} = 0.0933 \text{ A}, \quad (10)$$

$$I_{\text{bat,B}} = \frac{3.9575}{0.90 \cdot 12} = 0.3664 \text{ A}. \quad (11)$$

Battery Assumptions and SoC/DoD Limits

We consider a conventional automotive lead–acid battery of 60 Ah and 12 V as a representative mid-range value. Lead–acid battery capacity is commonly specified at standardized hour rates (e.g., 8 h, 10 h, 20 h), and this must be kept in mind when interpreting the nominal Ah rating [15].

The state of charge (SoC) is defined as the ratio between the remaining charge and the maximum deliverable charge, while the depth of discharge (DoD) is related by $\text{DoD} = 100\% - \text{SoC}$ [3]. Because reliable engine starting requires sufficient available power (especially at low temperature), automotive energy management strategies often keep the battery well above 70 % SoC to ensure start capability when the battery is in good condition [16]. Moreover, low temperature can degrade cold-cranking performance and available power, motivating conservative SoC margins in the 0 to 30 operating window [2]. Finally, deep discharges of starter batteries accelerate aging and are discouraged in practical usage [17, 6].

To include margin for temperature effects and battery aging, we adopt a conservative constraint

$$\text{SoC}_{\min} = 80\% \Rightarrow \text{DoD}_{\max} = 20\%. \quad (12)$$

Autonomy Results

Assuming a constant average load and neglecting second-order effects (self-discharge, converter quiescent current, cutoff-voltage constraints, and temperature-dependent capacity), the operating time is approximated by:

$$t \approx \frac{C_{\text{bat}} \cdot \text{DoD}}{I_{\text{bat}}}. \quad (13)$$

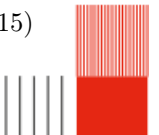
With $C_{\text{bat}} = 60 \text{ Ah}$ and $\text{DoD} = 0.20$, the usable charge is $C_{\text{usable}} = 12 \text{ Ah}$.

For Case A:

$$t_A = \frac{12}{0.0933} = 128.6 \text{ h} \approx 5.36 \text{ days}. \quad (14)$$

For Case B:

$$t_B = \frac{12}{0.3664} = 32.75 \text{ h} \approx 1.37 \text{ days}. \quad (15)$$



In a corporate fleet scenario with frequent vehicle usage, these autonomy bounds can be combined with operational policies (e.g., preventing extended vehicle-OFF periods without recharging) to ensure that the battery SoC does not fall below the conservative DoD = 20 % limit, thereby preserving reliable engine starting while supporting continuous keyless-access functionality.

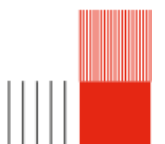
Smartphone Energy Considerations

The smartphone acts as the transmitter and user credential in our access workflow. However, unlike the vehicle-side nodes (which we can instrument directly on a fixed power supply), we are not able to perform a similarly detailed battery-autonomy study for the smartphone, since its consumption strongly depends on the device model, operating system behavior, background applications, and user habits.

In current smartphones, Bluetooth is typically enabled continuously and performs periodic advertising/scanning to discover and maintain connections with nearby devices. In our system, BLE can therefore be used as the default low-power “presence” layer: when proximity to the vehicle is detected, the access application can trigger UWB only for the short time window required to perform ranging and complete the access operation. From our measurements on the UWB platform, enabling UWB transmission increased the average current by about 17 mA compared with the non-transmitting state. In practice, this means that the energy impact of UWB on the smartphone side is mainly determined by *how long* UWB remains active: short ranging bursts lead to a limited additional battery drain, while continuously keeping UWB active would increase the average draw.

Moreover, many modern vehicles integrate wireless charging pads, so once the user enters the vehicle, the smartphone can be recharged during driving. This reduces the operational impact of the additional energy required by UWB-based access, since the energy spent during the short access phase can be compensated during normal usage of the vehicle.

Finally, our target scenario assumes a company-managed smartphone, which enables the deployment of device policies and application-level energy controls. As discussed by Chaib Draa, mobile energy consumption can be reduced by adapting system behavior to user needs and context, for instance by disabling unused peripherals and limiting non-essential background activities when they do not contribute to the user experience [4]. In our case, a similar approach can be implemented at the fleet-application level: when the user is far from any vehicle, the app remains in a low-activity state; when proximity is detected through BLE, UWB is enabled only for the minimal duration necessary to complete a secure ranging-based access procedure.



Fleet Operation and Energy Availability

Over the last few years, European countries have strengthened policy instruments to reduce transport-related carbon emissions, including incentives and tax schemes that affect vehicle purchase decisions and company-fleet composition. In particular, company-car taxation and recurring incentives have been shown to measurably influence the market shares of plug-in hybrid and battery-electric vehicles across European countries, highlighting the role of fiscal policy in accelerating fleet electrification [11].

In this work, the previous autonomy estimates were derived for a conventional low-voltage automotive supply (nominally 12 V), which remains a relevant baseline for internal-combustion vehicles and many hybrid architectures. Battery-electric vehicles (BEVs) generally rely on a high-voltage traction battery and an on-board DC-DC stage to supply the low-voltage bus and charge the 12 V battery; therefore, low-voltage loads may be supported differently depending on the vehicle power-management strategy and the vehicle state (driving, parked, sleep) [5].

Battery Constraints

For internal-combustion vehicles (ICEVs) and many hybrids, special attention must be given to the 12 V battery because it is closely tied to power-network stability and safety/availability of vehicle functions when the engine is off. Modern vehicles host a growing set of electrical loads, and low-voltage energy management is explicitly concerned with preventing insufficient supply to safety-critical functions under adverse conditions [13]. In our use case, an overly aggressive discharge of the starter battery could lead to two unacceptable outcomes: (i) the vehicle may not crank reliably, and (ii) the proposed keyless access function (BLE/UWB) would need to be shut down to preserve battery charge, defeating its operational purpose.

Mitigation Strategies

Even if the target fleet is expected to be frequently used (thus periodically recharging the 12 V system), robustness requires considering scenarios with prolonged parking (e.g., holiday periods, low-utilization assets, or operational disruptions). Two complementary mitigation strategies are therefore considered.

1. Auxiliary-battery autonomy example (LiFePO₄ 12.8 V – 30 Ah)

A practical way to protect the starter battery while keeping the access system available during long parking periods is to add a dedicated auxiliary battery. In our case, we consider, for example, the ECO-WORTHY LiFePO₄ battery shown in Figure 8, rated at 12.8 V and $C_{aux} = 30$ Ah.



Figure 8: Example of a dedicated auxiliary battery: ECO-WORTHY LiFePO₄ 12.8 V, 30 Ah.



For the auxiliary LiFePO₄ battery, the nominal voltage is $V_{\text{aux}} = 12.8 \text{ V}$ (instead of 12 V used for the starter-battery baseline). Therefore, the equivalent battery-side current must be recomputed using:

$$I_{\text{bat}} \approx \frac{P_{\text{tot}}}{\eta V_{\text{bat}}}, \quad V_{\text{bat}} = 12.8 \text{ V}. \quad (16)$$

With $\eta = 0.90$ and the same total load powers as previously derived ($P_{\text{tot},A} = 1.0075 \text{ W}$ and $P_{\text{tot},B} = 1.5075 \text{ W}$), we obtain:

$$I_{\text{bat},A} = \frac{1.0075}{0.90 \cdot 12.8} = 0.08746 \text{ A}, \quad (17)$$

$$I_{\text{bat},B} = \frac{3.9575}{0.90 \cdot 12.8} = 0.34353 \text{ A}. \quad (18)$$

As for the starter-battery analysis, we estimate the operating time using a constant average load and neglect second-order effects (self-discharge, converter quiescent current, cutoff-voltage constraints, and temperature dependence):

$$t \approx \frac{C_{\text{aux}} \cdot \text{DoD}_{\text{aux}}}{I_{\text{bat}}}. \quad (19)$$

Unlike the starter lead-acid battery, the auxiliary battery is dedicated to the standby electronics and does not need to preserve cold-start capability. Therefore, for LiFePO₄ we can reasonably use a deeper discharge. We take DoD_{aux} = 0.80 as a conservative usable fraction.

With $C_{\text{aux}} = 30 \text{ Ah}$, the expected autonomy becomes:

$$t_{A,\text{aux}} = \frac{30 \times 0.80}{0.08746} = 274.4 \text{ h} \approx 11.43 \text{ days}, \quad t_{B,\text{aux}} = \frac{30 \times 0.80}{0.34353} = 69.9 \text{ h} \approx 2.91 \text{ days}. \quad (20)$$

Compared to the 12 V baseline, the slightly higher nominal voltage of the LiFePO₄ battery reduces the battery-side current for a given load power, which marginally increases the autonomy.

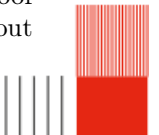
In this configuration, a 30 Ah LiFePO₄ auxiliary battery can sustain the access-system electronics for approximately 11.43 days in the BLE-only standby case (Case A) and 7.64 days in the worst-case continuous-UWB case (Case B), while keeping the starter battery untouched—an improvement from 5.36 to 11.43 days in Case A and from 1.37 to 2.91 days in Case B.

We consider this auxiliary unit because it is an automotive-grade battery that can be straightforwardly integrated into the vehicle wiring harness and charged from the existing low-voltage network (e.g., via the DC-DC/charge-control path), effectively acting as an add-on energy buffer. We focus on this solution precisely because it can be added to the vehicle with minimal architectural changes. Nevertheless, one could alternatively consider a higher-voltage lithium pack (e.g., a 30,000 mAh e-bike battery at 24–36 V); by repeating the same sizing calculations, a 30 Ah, 36 V pack could in principle extend the Case A autonomy beyond 30 days. However, charging such a pack and ensuring safe operation would require substantially tighter management (dedicated charging strategy, protection, and integration constraints), calling for a much more in-depth study.

2. Rooftop Solar Charging

Vehicle-integrated photovoltaics (VIPV) can be used as a practical *maintenance charger* for the vehicle low-voltage (12 V) battery while the car is parked. The key idea is to route the PV output through an automotive-grade charge controller (ideally with Maximum Power Point Tracking - MPPT) so that part of the harvested solar energy is stored in the 12 V battery. In this way, the PV system compensates (fully or partially) the standby consumption of the keyless-access electronics, preserving the battery state-of-charge and reducing the risk of reaching a “no-start” condition during extended parking periods [12, 9].

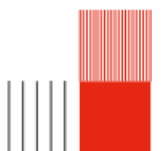
From the Vehicle-Integrated Photovoltaics perspective, the achievable roof power is limited primarily by available area and non-ideal orientation on curved surfaces. Schuss *et al.* report typical usable rooftop areas on the order of 1.5 m² to 2 m² and experimentally illustrate a 180 Wp-class installation on a Toyota Prius roof (45 mono-Si cells, ~1.1 m² cell area), while also highlighting that curvature and alignment can substantially reduce the effective output compared with a flat, optimally oriented panel [12]. Beyond peak power, the most relevant figure for battery preservation is the *daily energy* that can be harvested during parking. Based on solar-irradiation estimates from the European Commission’s Photovoltaic Geographical Information System (PVGIS) and including additional losses due to the roof curvature, Karoui *et al.* estimate that a curved passenger-car rooftop PV system would produce about



965 kWh/kWp/year in Paris and about 1535 kWh/kWp/year in Málaga; for a 180 kWp roof installation parked outdoors without shading, this corresponds to roughly a few hundred watt-hours of energy per day [8]. Real-world demonstrations further confirm that on-board PV can provide meaningful energy during daily parking, reducing external charging needs; for example, Masuda *et al.* report public-road tests of a Prius PHEV equipped with high-efficiency VIPV modules and show that outdoor parking periods can recharge the battery sufficiently to reduce plug-in charging frequency [10].

For our system-level requirement, the energy that must be “recovered” corresponds to the conservative starter-battery margin used in the autonomy analysis: 20 % DoD on a 60 Ah, 12 V battery (i.e., ≈ 12 Ah of charge headroom), which is approximately 0.14 kWh of battery energy. This amount is modest compared to the daily energy potentially available from a 180 kWp rooftop installation under clear-sky outdoor parking; therefore, in favorable conditions, a few effective sun-hours can plausibly replenish the 20 % margin within the same day. Even under less favorable conditions (partial shading, winter irradiance, non-optimal parking orientation), VIPV still improves robustness by slowing down the net discharge rate of the starter battery, thereby extending the safe parked duration before reaching the SoC limit.

Finally, it is important to note that PV energy cannot always be fully stored: if the battery is already near full, part of the potential solar harvest is curtailed (the “full-battery effect”), which motivates maintaining sufficient SoC headroom and/or ensuring some daytime load so that harvested energy is not wasted [9]. Overall, rooftop PV should be viewed as a strong *battery-preservation* mechanism that can maintain keyless-access availability during long parking periods, rather than as a guaranteed sole power source under all parking scenarios [12, 1].



Conclusion

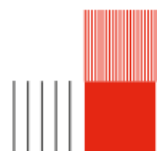
This report presented an energy-focused study of a keyless-access architecture combining BLE for low-power presence detection and UWB for short, accurate ranging phases. From the experimental measurements (power-analyzer baseline and shunt-resistor oscilloscope setup), the main observation is that energy cost is primarily driven by the *duty cycle* of communication events. On the initiator side, UWB exchanges generated current peaks at a constant 200 ms period (5 Hz), confirmed both in the execution logs and on the oscilloscope. On the responder side, the effective update period varied with link conditions from approximately 200 ms to 500 ms, consistent with the non-uniform spacing between reception-related current peaks.

Using a conservative vehicle-side constraint ($\text{SoC}_{\min} = 80\%$, i.e., $\text{DoD} = 20\%$) to preserve reliable starts in the 0 to 30 window [2, 17, 16], we estimated the parked autonomy of a 60 Ah starter battery under two operating cases. In the BLE-only standby case, the system can operate for approximately 5.36 days, whereas a worst-case continuous-UWB scenario reduces the autonomy to about 3.58 days. This leads to a clear design guideline: UWB should remain *event-driven* and enabled only for the short time window required to complete access/ranging, while BLE is used as the default low-energy trigger layer [7].

On the smartphone side, a detailed battery-autonomy analysis is outside the scope of this work because consumption depends on the device, operating system behavior, and user context. Nevertheless, UWB activity is bursty, so its impact is mainly determined by activation time. In the corporate-fleet scenario, the smartphone can be company-managed, enabling policies and context-aware controls to reduce unnecessary background activity [4]. In addition, many vehicles include wireless charging pads, which can compensate the short access-related energy expenditure once the user is inside the car.

Two mitigation strategies can further increase robustness during long idle periods. First, an auxiliary battery can decouple the access electronics from the starter battery and preserve cold-start capability. Second, rooftop photovoltaic charging can act as a maintenance charger during outdoor parking: vehicle-integrated PV studies indicate that rooftop systems can harvest a few hundred watt-hours per day depending on location, season, and curvature/shading losses [12, 8]. However, effectiveness depends strongly on parking conditions and may be limited when the battery is already near full [9].

As future work, three directions are relevant: (i) hardware/firmware optimization (minimal PCB and deeper sleep strategies), (ii) energy-aware control integrated with low-voltage energy management [13], and (iii) deployment in electrified fleets, where low-voltage loads are supplied through the traction battery via an on-board DC–DC converter [5]. In corporate depots, parked electric vehicles are often connected to the grid, which reduces the risk of energy unavailability while the same optimization principles remain beneficial to minimize parasitic losses.



Bibliography

- [1] Kenji Araki, Liang Ji, George Kelly, and Masafumi Yamaguchi. To do list for research and development and international standardization to achieve the goal of running a majority of electric vehicles on solar energy. *Coatings*, 8(7):251, 2018.
- [2] Sophia Bauknecht, Florian Wätzold, Anton Schlösser, and Julia Kowal. Comparing the cold-cranking performance of lead-acid and lithium iron phosphate batteries at temperatures below 0 °c. *Batteries*, 9(3):176, 2023.
- [3] BioLogic Learning Center. What are soc and soh of a battery, how to measure them? Web page, October 2024. Accessed: 2026-01-16.
- [4] Ismat Chaib Draa. *Optimisation de la consommation d'énergie des systèmes mobiles par l'analyse des besoins de l'utilisateur*. Phd thesis, Université de Valenciennes et du Hainaut-Cambresis, 2018. HAL Id: tel-02127928v1.
- [5] Sajib Chakraborty, Hai-Nam Vu, Mohammed Mahedi Hasan, Dai-Duong Tran, Mohamed El Baghdadi, and Omar Hegazy. Dc-dc converter topologies for electric vehicles, plug-in hybrid electric vehicles and fast charging stations: State of the art and future trends. *Energies*, 12(8):1569, 2019.
- [6] Miguel Franco Rius. Influence of shallow cycling on the ageing of sli batteries. Master's thesis, Universitat Politècnica de Catalunya (UPC), 2010. Accessed: 2026-01-16.
- [7] Eduardo Garcia-Espinosa, Omar Longoria-Gandara, Ivan Pegueros-Lepe, and Alfredo Veloz-Guerrero. Power consumption analysis of bluetooth low energy commercial products and their implications for iot applications. *Electronics*, 7(12):386, 2018.
- [8] Fathia Karoui, Bertrand Chambion, Fabrice Claudon, and Benjamin Commault. Integrated photovoltaics potential for passenger cars: A focus on the sensitivity to electrical architecture losses. *Applied Sciences*, 13(14):8373, 2023.
- [9] Chiara Lodi, Susana Gil-Sayas, Davide Currò, Simone Serra, and Yannis Drossinos. Full-battery effect during on-board solar charging of conventional vehicles. *Transportation Research Part D: Transport and Environment*, 96:102862, 2021.
- [10] Taizo Masuda, Masafumi Yamaguchi, Shinya Iwasaki, Takashi Nakado, Tatsuya Takamoto, and Kensuke Nishioka. Public road driving tests of toyota prius equipped with high-efficiency iii-v triple-junction pv modules. *EPJ Photovoltaics*, 16:20, 2025.
- [11] Hendrik Schub, Patrick Plötz, and Frances Sprei. Electrifying company cars? the effects of incentives and tax benefits on electric vehicle sales in 31 european countries. *Energy Research & Social Science*, 120:103914, 2025.
- [12] Christian Schuss, Tapio Fabritius, Bernd Eichberger, and Timo Rahkonen. Calculating the output power of photovoltaic cells on top of electric and hybrid electric vehicles. In *2019 IEEE International Instrumentation and Measurement Technology Conference (I2MTC)*, pages 1–6, Auckland, New Zealand, 2019. IEEE.
- [13] Ömer Tan, Daniel Jerouschek, Ralph Kennel, and Ahmet Taskiran. Energy management strategy in 12-volt electrical system based on deep reinforcement learning. *Vehicles*, 4(2):621–638, 2022.
- [14] Texas Instruments. Tpsm33620-q1: 3 v to 36 v input, 1 v to 7 v output automotive synchronous buck converter power module (product page). Web page. Accessed: 2026-01-16.



- [15] U.S. Department of Energy. *DOE-HDBK-1084-95: Primer on Lead-Acid Storage Batteries*, 1995. Accessed: 2026-01-16.
- [16] VARTA Automotive. Start-stop myths. Web page. Accessed: 2026-01-16.
- [17] ZVEI – German Electrical and Electronic Manufacturers' Association. Lead-acid starter batteries in systems: Usage information. Information leaflet 28e, ZVEI Batteries Association (Working Group Starter Batteries), October 2017. Edition October 2017. Accessed: 2026-01-16.

